Available online at www.sciencedirect.com
SCIENCE DIRECT®
Comput. Methods Appl. Mech. Engrg. 193 (2004) 2699–2718
Computer methods in applied mechanics and engineering
www.elsevier.com/locate/cma

Computational modeling of deformation bands in granular media. II. Numerical simulations

Ronaldo I. Borja *

Department of Civil and Environmental Engineering, Stanford University, Stanford, CA 94305-4020, USA

Received 9 May 2003; received in revised form 12 September 2003; accepted 14 September 2003

Abstract

Development of accurate mathematical models of geomaterial behavior requires a more fundamental understanding of the localization phenomena; in particular, the important factors responsible for the inception and development of localized deformation. The objective of this paper is to implement and test the mathematical formulations presented in a companion paper to better understand the different failure processes in granular media, specifically the formation of deformation bands in geomaterials. Our approach revolves around the use of classical bifurcation theory combined with advanced constitutive modeling and state-of-the-art computation to capture the end members of the failures modes described in the companion paper, namely, simple shear, pure compaction, and pure dilation bands, as well as the combination modes described in the geological framework. The paper revisits the notion of the critical hardening modulus as it applies to the entire range of failure modes, elucidates the role of the third stress invariant and finite deformation effects on the localization properties, and describes some useful properties of the constitutive and algorithmic tangent operators as they relate to the capture of the onset of deformation bands in geomaterials.

Keywords: Deformation bands; Granular media

1. Introduction

Recently, a classification scheme that accounts for the entire spectrum of failure processes in the form of tabular deformation bands has been proposed for geologic media [1,2]. The failure modes are composed of three end members: pure compaction, simple shear, and pure dilation. In addition, two combination localized failure modes that have been documented to be the most common in granular media have been identified, namely, compactive shear band and dilatant shear band. The micromechanics of failure depends on interplay among grain boundary sliding, pore enlargement or collapse, and grain fracturing, controlled in large part by the petrophysical properties of the granular materials and the loading conditions [2–5].

* Fax: +1-650-723-7514.
E-mail address: borja@stanford.edu (R.I. Borja).

0045-7825/$ - see front matter
doi:10.1016/j.cma.2003.09.018

Classical bifurcation theory [6] along with the use of more realistic constitutive models [7–9] are essential for capturing localized failure in the form of tabular deformation bands in granular media. In the companion paper [1], this theory also has been utilized to analyze the more intriguing failure modes called pure compaction band [10,11] and pure dilation band [12] in which deformations are predominantly volumetric and lack a characteristic shear offset. The mathematical analysis revolves around the condition that the traction vector be continuous across the band, leading to a homogeneous system of equations. Depending on the position of the stress point on the yield surface at the moment of localization, it has been shown that any of the failure modes identified in the geological framework is possible [1].

The objective of this paper is to investigate the onset of tabular deformation bands in granular media using the family of three-invariant elastoplastic constitutive models described in the companion paper as the basis material model. In order to constrain the parameters of the constitutive model, we utilize the results of Lade and Kim [13–15] and use specific values of model parameters for different granular materials including soils, rocks, and plain concrete [13–15]. With extensive numerical simulations we show that a pure compaction band can develop over a wide range of values of stresses. We also describe a so-called transition failure mode from a pure compaction band to a compactive shear band, where the localization condition is satisfied over a relatively broad range of possible band orientations. In a sense, this transition mode is analogous in meaning to the idea advanced in [16] that the transition from a pure compaction band to a compactive shear band, expressed through the so-called critical plastic modulus, is continuous.

We also compare the localization properties of the constitutive and algorithmic tangent operators for predicting the onset of tabular deformation bands over the entire spectrum of failure modes. We show that the two tangent operators can be used interchangeably to predict the onset of localization, a computational advantage since this implies that we can completely dispense with the constitutive tangent operator in the calculations. Finally, we compare the predictions of the small strain and finite deformation models to better understand the importance of geometric nonlinearity on the capture of localized failure processes in granular media.

2. Pure compaction and compactive shear bands

Kim and Lade [13–15] proposed a yield function for geomaterials of the form

$$F = \psi(f_1 + c_3 f_3)^{\mu}\bar{I}_1 + \kappa = 0, \quad f_1 = \bar{I}_1^2/\bar{I}_2, \;\; f_3 = \bar{I}_1^3/\bar{I}_3, \tag{2.1}$$

where $\bar{I}_1$, $\bar{I}_2$, and $\bar{I}_3$ are the invariants of the translated principal stresses $\bar{\sigma}_1 = \sigma_1 - a$, $\bar{\sigma}_2 = \sigma_2 - a$, and $\bar{\sigma}_3 = \sigma_3 - a$, ψ is an exponential function of the stresses, a is a cohesion-like parameter describing the distance of the vertex of F from the origin of the principal stress axes, and $\kappa < 0$ is a stress-like plastic internal variable conjugate to the plastic volumetric strain. The shape of this yield function has been inferred from contours of constant plastic work over a wide range of confining stresses for many geomaterials. If we take ψ to be a constant, then the above function becomes a special case of the more general family of yield surfaces presented in [1] in which $c_0 = 0$, $c_1 = 1$ and $c_2 = 0$. Typical values of $c_3 = 0.0013$ and $\mu = 0.5$ have been reported in [13] for sandstone and plain concrete based on data reported in [17–20].

Fig. 1 shows a three-dimensional plot of the yield surface in translated principal stress space. The surface has the shape of an asymmetric teardrop with a vertex at the origin of the translated principal stress axes. Fig. 2 shows plots of the yield surfaces on a meridian plane for different values of κ (in kPa). For pure hydrostatic compression characterized by $f_1 = 3$ and $f_3 = 27$, the relationship between $\bar{I}_1$ and the parameter κ is $\bar{I}_1 = 0.574\kappa$. The rotated axes σ_1'', σ_2'' and σ_3'' were obtained by performing a sequence of rotations relative to the translated principal stress axes in accordance with the relationships described in Appendix A of [8] and shown once again in Fig. 3; the plots shown in Fig. 2 then correspond to the meridian plane $\sigma_1'' = 0$. The rotated axis σ_3'' coincides with the hydrostatic axis, and for pure hydrostatic compression we

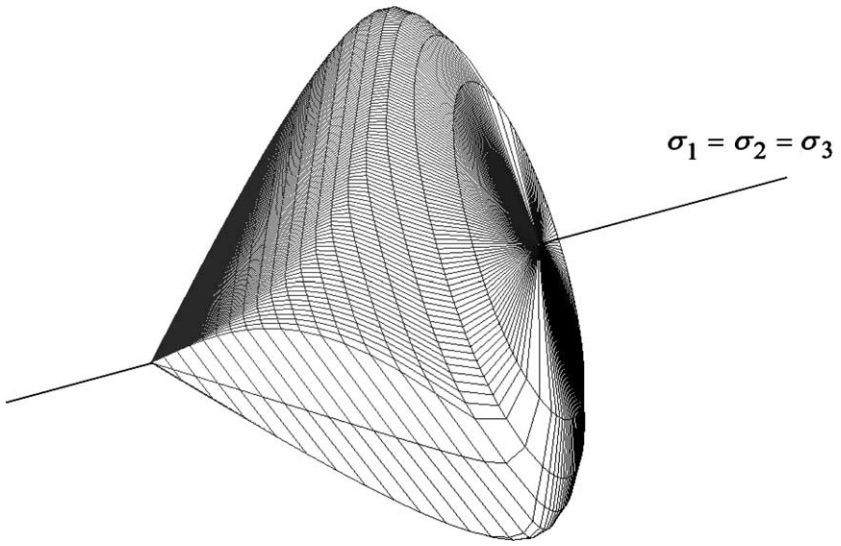

Fig. 1. Yield surface for sandstone.

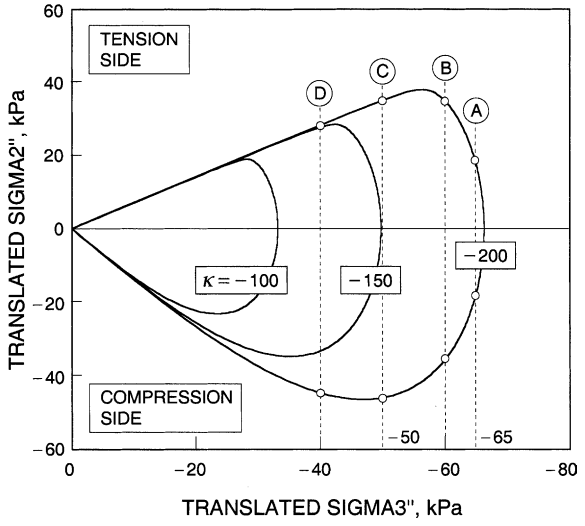

Fig. 2. Yield surfaces for sandstone on meridian plane ($\sigma_1'' = 0$).

have the relationships $\bar{I}_1 = \sqrt{3}\sigma_3''$ and $\sigma_3'' = 0.331\kappa$. Figs. 1–3 show that the cross-sections of the yield surfaces are nearly circular at high confining pressures and nearly triangular at low confining pressures. Hardening/softening changes the size of the yield surface in a way that very much resembles the motion of a compression cap, as in the plasticity model of DiMaggio and Sandler [21].

From the directions of plastic strain increments, Kim and Lade [13] proposed a plastic potential function of the form

$$G = (-\bar{c}_0 + f_1 + c_3 f_3)^v \bar{I}_1. \tag{2.2}$$

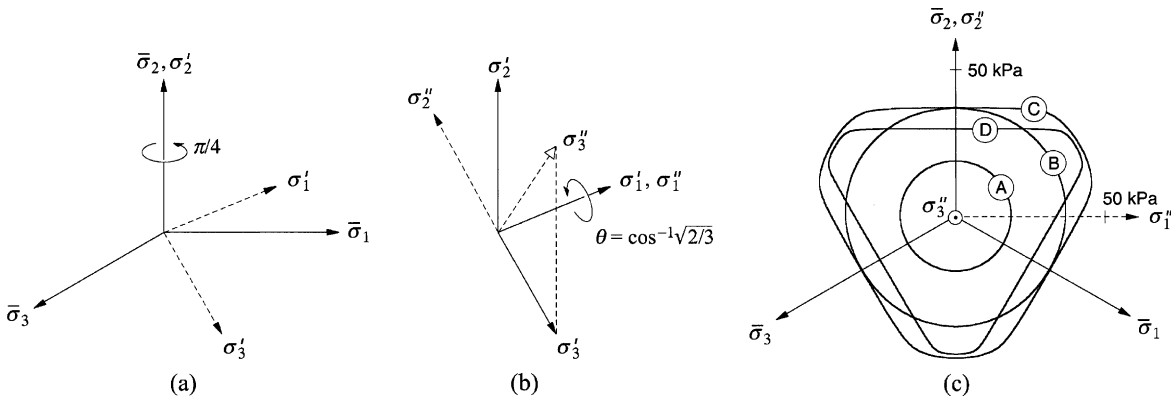

Fig. 3. Sequence of rotation of translated principal stress axes and cross-sections of yield surface on deviatoric plane.

Once again, the above expression is a special case of the more general family of plastic potential functions presented in [1], with $c_1 = 1$ and $c_2 = 0$. A value of $c_3 = 0.0013$ is typical for sandstone and plain concrete [17,18,20,22]. No values of $\bar{c}_0$ and v have been reported for sandstone, but for plain concrete these parameters have typical values of about $c_0 = 3.0$ and $v = 0.25$ [13]. The parameter $\bar{c}_0$ changes the shape of the plastic potential function from that of a teardrop ($\bar{c}_0 = 0$) to that of a cigar ($\bar{c}_0 > 0$), see Fig. 4. In the following simulations we shall use the parameter $\bar{c}_0$ to demonstrate the dependence of the localization theory on the constitutive properties of the material. Throughout the simulations we shall assume $E = 100$ MPa (Young's modulus), $\bar{\nu} = 0.20$ (Poisson's ratio) and $a = 10$ kPa (cohesion-like parameter).

2.1. Pure compaction band

The simulation of the formation of pure compaction bands at the stress-point level consists of the following imposed local strain history: $\Delta\epsilon_{11} = -0.01\%$, all other $\Delta\epsilon_{ij}'s = 0$. The element is thus subjected to a one-dimensional constrained compression. We shall take the initial stresses as $\sigma_{11} = \sigma_{22} = \sigma_{33} = -100$ kPa (isotropic). The variable κ is assumed to vary according to the expression

$$\kappa = a_1 v^{\mathrm{p}} \exp(a_2 v^{\mathrm{p}}), \tag{2.3}$$

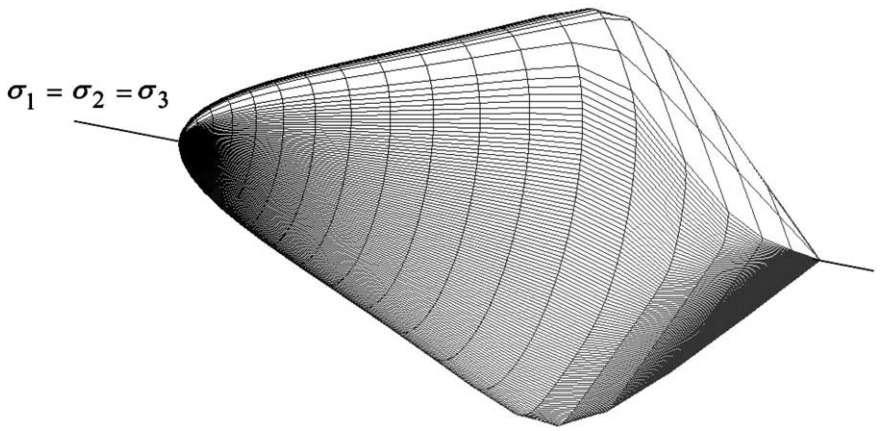

Fig. 4. Plastic potential surface for sandstone.

where $a_1 = 200$ MPa and $a_2 = 100$; with initial values $v_0^{\mathrm{p}} = -0.5\%$ and $\kappa_0 = -606$ kPa. Softening takes place at a value of $v^{\mathrm{p}} = -1/a_2 = -1\%$.

With $\bar{c}_0 = 0$, Fig. 5 shows a pure compaction band forming at a cumulative strain $\epsilon_{11} = -0.28\%$. The band orientations at the bifurcation point where the determinant function vanishes for the first time are 0° and 180° (Fig. 5a and b), and in order for plastic yielding to persist inside the band, $\boldsymbol{m} \cdot \boldsymbol{n} = -1$. At the localization point $a_{AA}^{\mathrm{ep}} = 0$ for $A = 1$, but remains positive for $A = 2, 3$ (Fig. 5c). The vanishing of a_{11}^{ep} thus affirms the formation of a pure compaction band. Furthermore, the critical plastic modulus for this particular failure mode is

$$H_{\mathrm{cr}} = h_A = \left(K + \frac{4\mu}{3}\right)^{-1} \tilde{q}_A \tilde{f}_A - \bar{\chi}, \tag{2.4}$$

and for $A = 1$ this equals the hardening modulus at localization. Note in this case that localization takes place in the hardening regime defined by $H > 0$ (Fig. 5d).

Beyond the localization point we also plot in Fig. 5d the variation of the critical hardening modulus H_{cr} over the entire range of deformation. This parameter defines the value of H at which the minimum of the determinant function vanishes [6]. For complex models such as the ones considered in this paper,

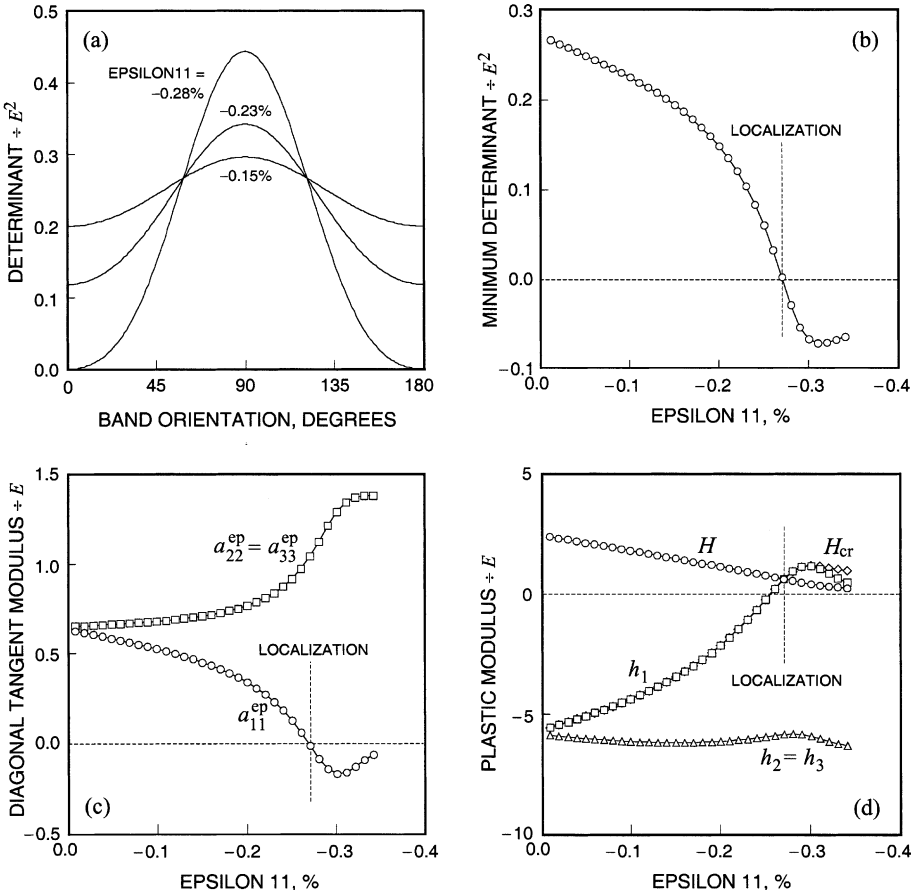

Fig. 5. Pure compaction band, $\bar{c}_0 = 0$.

closed-form solutions for H_{cr} are difficult to find, and thus we resort to numerical calculations to determine the variation of this function with imposed deformation. A simple algorithm would be to start out with the actual value of H and search the minimum of the determinant function by sweeping across the entire range of possible band orientations. If this minimum is positive (negative), then H is decreased (increased) until a certain small threshold absolute value is reached. Fig. 5d shows that for a pure compaction band $H_{cr} = h_1$ up until the onset of localization, but at a more advanced stage of loading H_{cr} diverges from h_1.

With $\bar{c}_0 = 3$, which is typical for many geomaterials, Fig. 6 shows a pure compaction band developing at a cumulative plastic strain $\epsilon_{11} = -0.52\%$. This strain level is nearly twice larger than the one predicted earlier using the parameter value $\bar{c}_0 = 0$, and well demonstrates the strong dependence of the localization model on the constitutive model parameters.

2.2. Transition from pure compaction band to compactive shear band

There exists a transition point at which a pure compaction band becomes a compactive shear band, and the following example illustrates this particular transition mode. The simulation consists of prescribing the following local strain history: $\Delta\epsilon_{11} = -0.01\%$, $\Delta\epsilon_{22} = 0.0025\%$, all other $\Delta\epsilon_{ij}'s = 0$. The element is thus subjected to plane strain compression and stretching in the 1- and 2-directions, respectively.

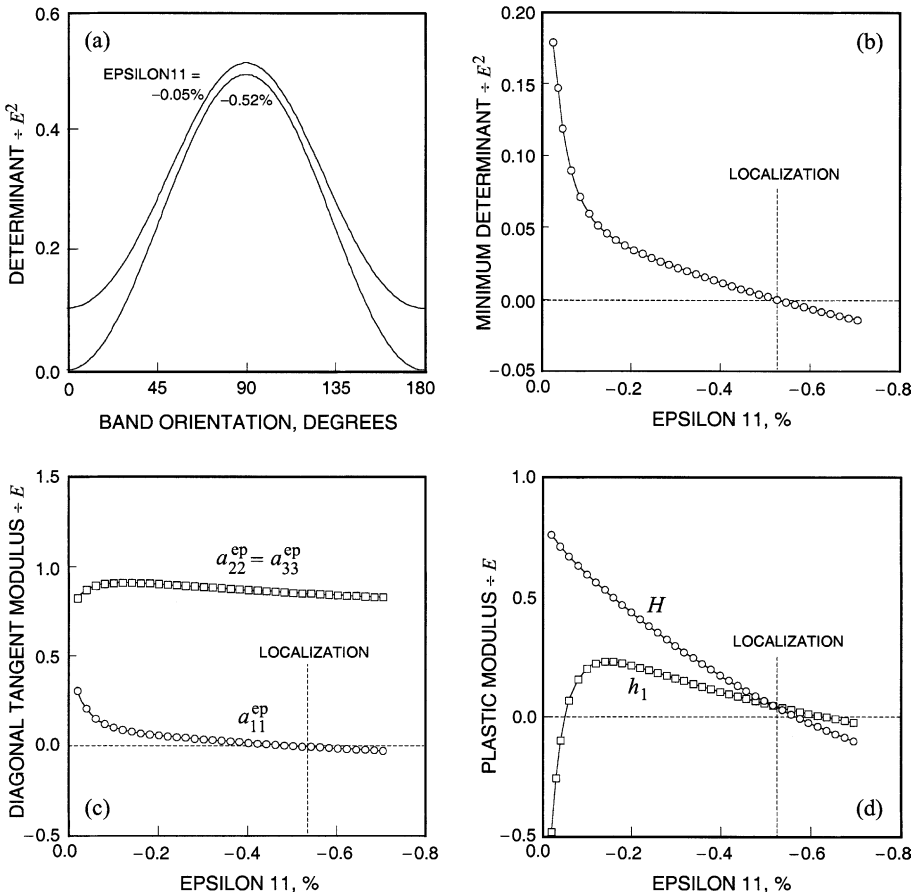

Fig. 6. Pure compaction band, $\bar{c}_0 = 3$.

Using the same model parameters as in the previous example (with $\bar{c}_0 = 0$), Fig. 7 shows the transition mode from a pure compaction band to a compactive shear band. Localization is predicted at a cumulative strain $\epsilon_{11} = -0.22\%$ where the band orientations are 0° and 180° (Fig. 7a and b). Note that there is a wide range of band orientations where the determinant function is flat and where the value of the determinant is nearly zero (Fig. 7a). Theoretically, any band oriented at $|\theta| < \bar{\theta}$, where $\bar{\theta}$ is defined in Fig. 7a, is a potential deformation band. The diagonal elements of the elastoplastic matrix $[a^{ep}_{AB}]$ are also plotted in Fig. 7c, showing a^{ep}_{11} just grazing the zero value at the localization point. The simulations also show that the parameters h_1 and H_{cr} are the same at the initial stage of loading up until the bifurcation point, but deviate from each other thereafter (Fig. 7d). Note that if $\Delta\epsilon_{22}$ had been less than the above assumed value a pure compaction band would still form, demonstrating that this particular failure mode is not limited to the case of one-dimensional constrained compression.

2.3. Compactive shear band

Fig. 8 shows a compactive shear band forming following the imposed local strain history $\Delta\epsilon_{11} = -0.01\%$, $\Delta\epsilon_{22} = 0.004\%$, all other $\Delta\epsilon_{ij}'s = 0$. Localization occurs at a cumulative strain $\epsilon_{11} = -0.21\%$ at band

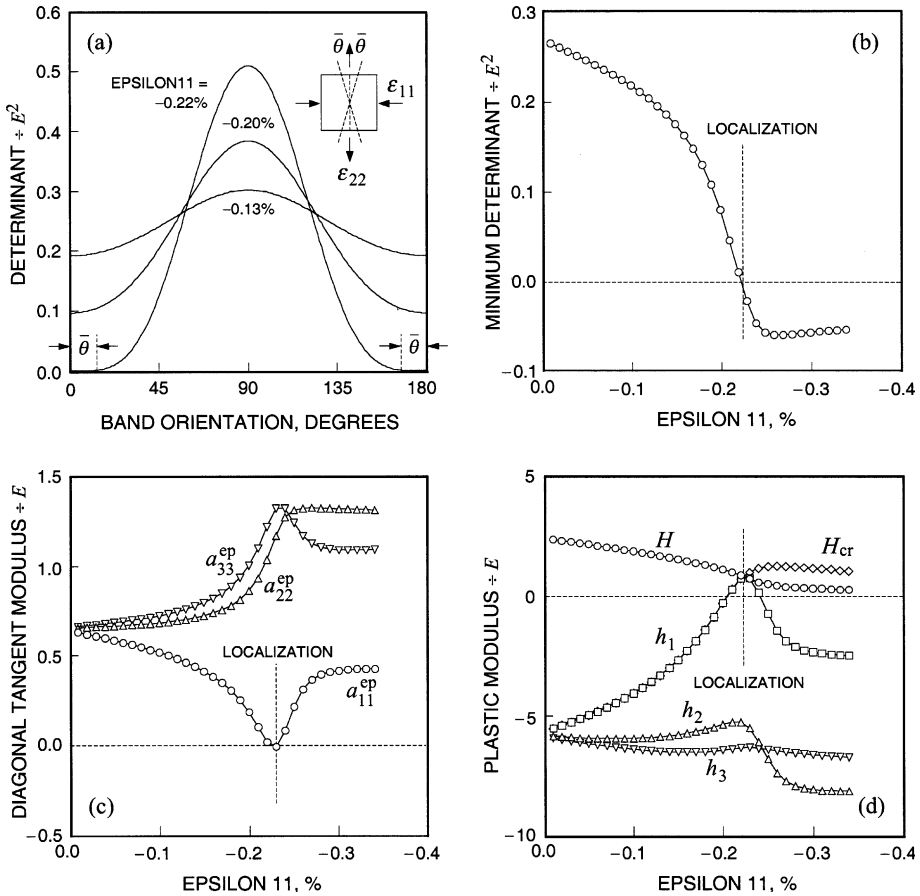

Fig. 7. Transition from pure compaction band to compactive shear band.

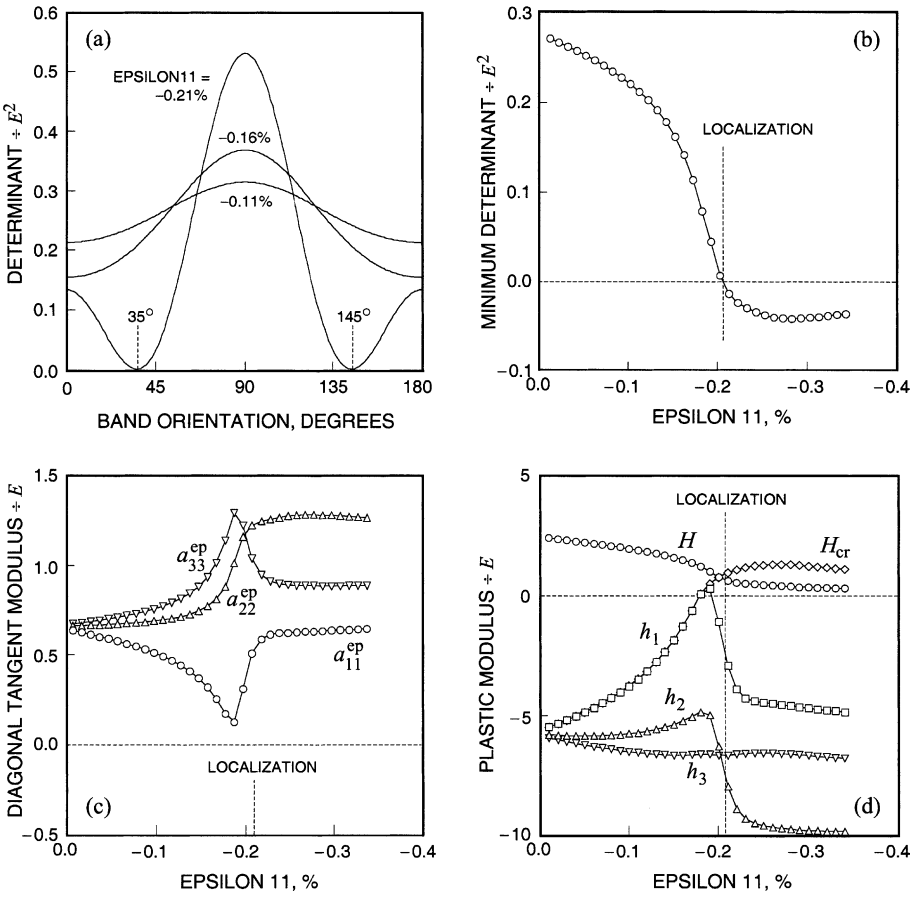

Fig. 8. Compactive shear band.

orientations of 35° and 145° (Fig. 8a and b), where the orientations of the corresponding unit eigenvectors $\boldsymbol{m}$ are 157° and 23°, respectively. Thus, the angle between $\boldsymbol{n}$ and $\boldsymbol{m}$ is 122° for either case, and $\boldsymbol{m} \cdot \boldsymbol{n} = -0.53$ implying a compactive shear band. Throughout the entire loading history no diagonal element of the elastoplastic matrix $[a^{\mathrm{ep}}_{AB}]$ became zero (Fig. 8c), and all h_A's were less than the actual plastic modulus H (Fig. 8d). The numerically calculated critical plastic modulus H_{cr} crosses the actual plastic modulus at the localization point.

The transition from a pure compaction band to a compactive shear band is elucidated further in Fig. 9 in the context of the combined plane strain compression–extension simulations. At a strain ratio of around $\epsilon_{22}/\epsilon_{11} = -0.25$ the orientation of the unit normal vector $\boldsymbol{n}$ begins to deviate from zero to define a compactive shear band. At this same moment the scalar product $\boldsymbol{m} \cdot \boldsymbol{n}$ increases above the value -1.0 albeit the angle between the two vectors remains obtuse. Note in Fig. 9b the steep variation of the orientation angle θ within this transition zone defined by the range $0 < \theta < \bar{\theta}$. This is due to the broad band orientation angles in Fig. 7a where the determinant function is flat throughout and having a value nearly equal to zero (see the plot for $\epsilon_{11} = -0.22\%$), implying that the orientation of $\boldsymbol{n}$ could be anywhere within this range of possible band orientations and still satisfy the localization condition.

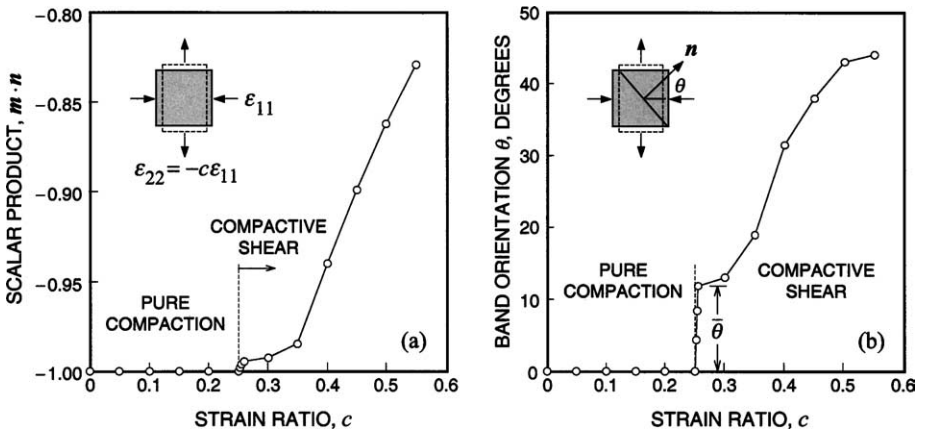

Fig. 9. Transition from pure compaction band to compactive shear band.

2.4. Localization properties of constitutive and algorithmic tangent operators

We recall the spectral representation of the constitutive elastoplastic tangent operator [1]

$$\boldsymbol{c}^{\mathrm{ep}} = \sum_{A=1}^{3}\sum_{B=1}^{3} a_{AB}^{\mathrm{ep}} \boldsymbol{m}^{(A)} \otimes \boldsymbol{m}^{(B)} + \frac{1}{2}\sum_{A=1}^{3}\sum_{B\neq A}\left(\frac{\sigma_B - \sigma_A}{\epsilon_B^{\mathrm{e}} - \epsilon_A^{\mathrm{e}}}\right)(\boldsymbol{m}^{(AB)} \otimes \boldsymbol{m}^{(AB)} + \boldsymbol{m}^{(AB)} \otimes \boldsymbol{m}^{(BA)}), \tag{2.5}$$

and the spectral representation of the algorithmic tangent operator

$$\boldsymbol{c} = \sum_{A=1}^{3}\sum_{B=1}^{3} a_{AB} \boldsymbol{m}^{(A)} \otimes \boldsymbol{m}^{(B)} + \frac{1}{2}\sum_{A=1}^{3}\sum_{B\neq A}\left(\frac{\sigma_B - \sigma_A}{\epsilon_B^{\mathrm{e\,tr}} - \epsilon_A^{\mathrm{e\,tr}}}\right)(\boldsymbol{m}^{(AB)} \otimes \boldsymbol{m}^{(AB)} + \boldsymbol{m}^{(AB)} \otimes \boldsymbol{m}^{(BA)}). \tag{2.6}$$

The spectral directions $\boldsymbol{m}^{(A)}$, $\boldsymbol{m}^{(B)}$, $\boldsymbol{m}^{(AB)}$, and $\boldsymbol{m}^{(BA)}$ are the same for both operators. Thus, $\boldsymbol{c}$ differs from $\boldsymbol{c}^{\mathrm{ep}}$ only through the material tangent coefficient matrix $[a_{AB}]$ and the rotational coefficients $1/(\epsilon_B^{\mathrm{e\,tr}} - \epsilon_A^{\mathrm{e\,tr}})$.

The properties of the two tangent operators with respect to the prediction of the bifurcation point are depicted in Fig. 10 for pure compaction band and compactive shear band failure modes (with $\bar{c}_0 = 0$). For the pure compaction band simulation the diagonal elements of $[a_{AB}^{\mathrm{ep}}]$ and $[a_{AB}]$ are nearly the same prior to localization, leading to the same bifurcation point (Fig. 10a). A similar statement can be made for the transition failure mode (Fig. 10b). For the compactive shear band mode the diagonal elements of $[a_{AB}^{\mathrm{ep}}]$ and $[a_{AB}]$ are not quite the same, but it must be recalled they do not alone determine the localization condition. Including the rotational components of the tangent operators the predicted bifurcation points are also nearly the same as shown in Fig. 10d. We emphasize that the localization condition is expressed in terms of $\boldsymbol{c}^{\mathrm{ep}}$ and not of $\boldsymbol{c}$, but the results shown above suggest that $\boldsymbol{c}$ can very well be used in lieu of $\boldsymbol{c}^{\mathrm{ep}}$ for localization calculations.

In conclusion, the algorithmic tangent operator $\boldsymbol{c}$ appears to be an acceptable approximation of the constitutive tangent operator $\boldsymbol{c}^{\mathrm{ep}}$ for purposes of identifying the bifurcation points. This is true both for pure compaction and mixed mode deformation bands. As an aside, it is well known that $\boldsymbol{c}^{\mathrm{ep}}$ is generally not an acceptable approximation of $\boldsymbol{c}$ for nonlinear calculations with Newton's method [23]. Thus, the algorithmic tangent operator $\boldsymbol{c}$ appears sufficient both for deformation and localization calculations. Finally, pure compaction band failure modes are influenced only by the material tangent stiffness matrix $[a_{AB}^{\mathrm{ep}}]$ (approximated by the algorithmic tangent stiffness $[a_{AB}]$), whereas shear band failure modes are influenced both by the material and rotational components of the tangent operator.

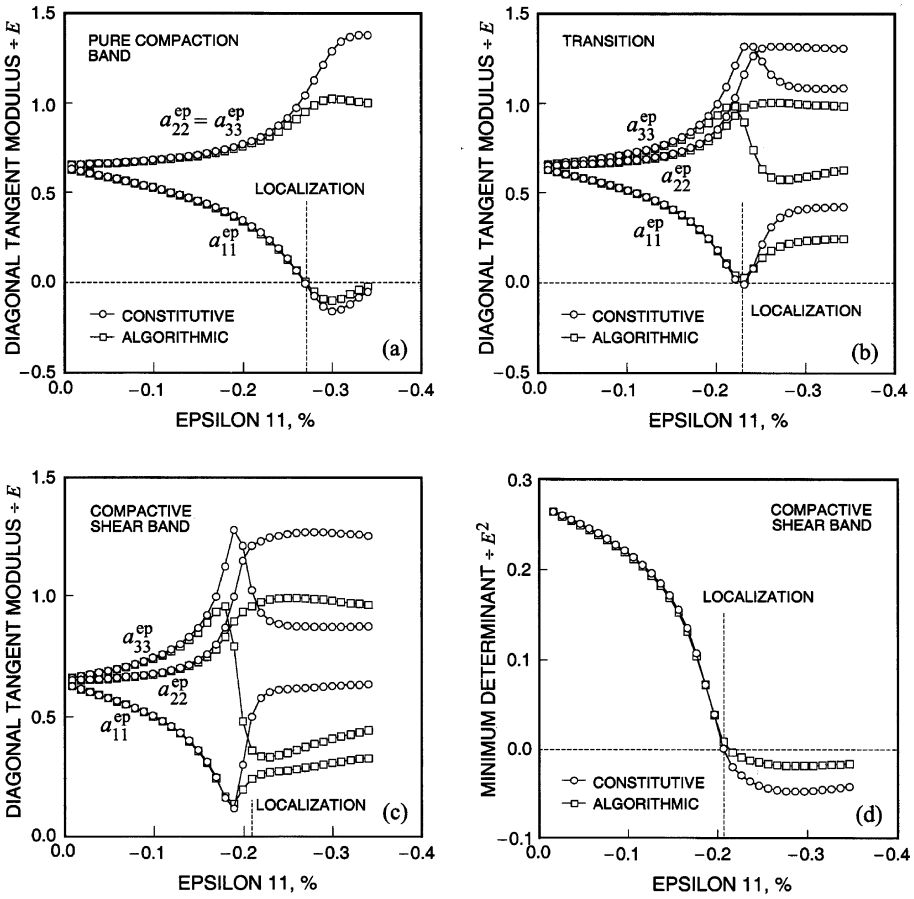

Fig. 10. Properties of constitutive and algorithmic tangent operators relevant to localization analysis.

3. Isochoric and dilatant shear bands

We investigate two more failure modes identified in the geological framework of [1], namely, isochoric (simple) shear bands and dilatant shear bands.

3.1. Isochoric (simple) shear band

Two different shear modes may be applied to an elementary volume on the plane 12 to capture an isochoric shear band failure mode, namely, a volume-preserving plane strain compression/stretching and a volume-preserving plane strain simple shearing. Desrues and Chambon [24] used the terms "in-axes" and "out-of-axes" shearing for these two shear modes, respectively.

Fig. 11 shows the formation of an isochoric shear band from the following imposed "in-axis" local shearing: $\Delta\epsilon_{11} = -\Delta\epsilon_{22} = -0.01\%$, all other $\Delta\epsilon_{ij}'s = 0$. The material model and initial conditions are the same as in the previous examples (assuming $\bar{c}_0 = 3$). Note that the imposed deformations are volume preserving but the plastic flow is not necessarily isochoric particularly during initial stages of loading when the stress point was near the hydrostatic axis. However, as deformation progresses plastic flow becomes more and more volume preserving as manifested by the plastic modulus H becoming nearly a constant

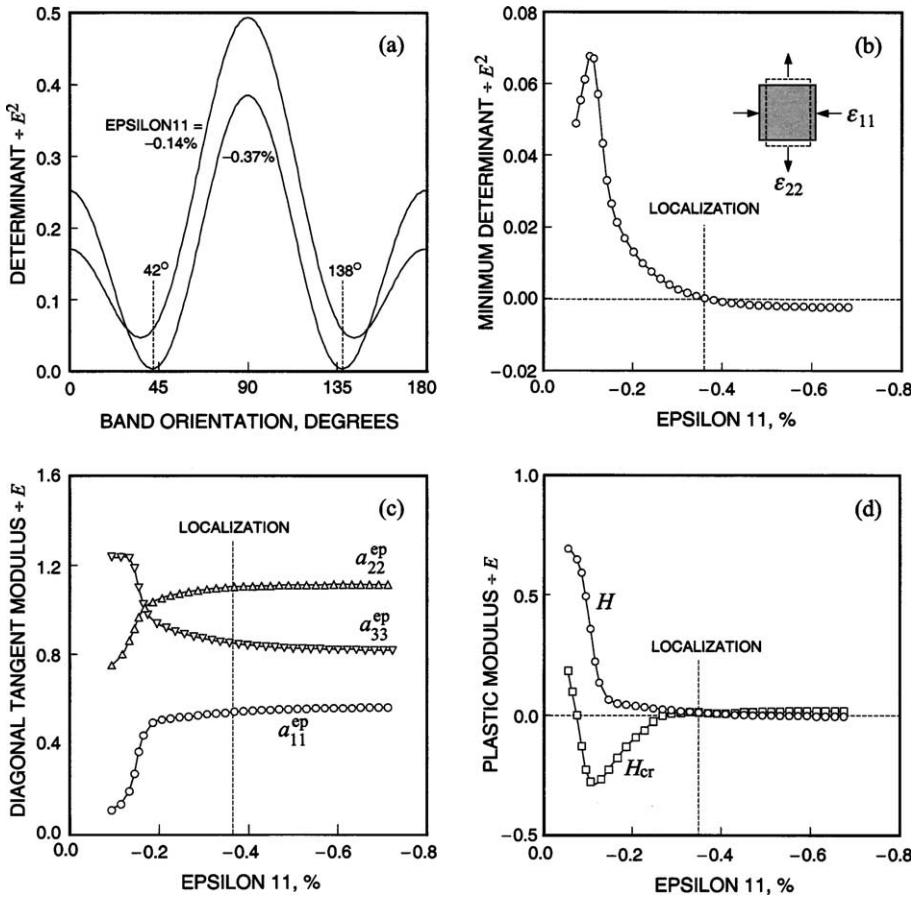

Fig. 11. Simple shear band, "in-axes" shear mode.

function of ϵ_{11}, suggesting that the cumulative plastic volumetric strain v^{p} is nearly constant at a more advanced stage of loading.

Localization is detected at a cumulative strain $\epsilon_{11} = -0.37\%$ at band orientations of 42° and 138° (orientations of $\boldsymbol{n}$ with respect to the positive 1-axis). At the localization point the plastic modulus H is nearly flat, implying that v^{p} is nearly constant (and thus the element flows plastically at a constant volume). For the band orientation of 42° the orientation of $\boldsymbol{m}$ is 134°, while for the band orientation of 138° the orientation of $\boldsymbol{m}$ is 46°; in both cases, the angle between $\boldsymbol{n}$ and $\boldsymbol{m}$ is 92°, and thus $\boldsymbol{m} \cdot \boldsymbol{n} = -0.03 \approx 0$, implying that $\boldsymbol{m}$ is nearly perpendicular to $\boldsymbol{n}$ (albeit the shear band still exhibits a slight compaction). The diagonal elements of the matrix $[a^{\mathrm{ep}}_{AB}]$ are all positive and never crossed the value zero.

Fig. 12 shows the formation of a similar isochoric shear band from the following imposed "out-of-axis" local shearing: $\Delta\gamma_{12} = 2\,\Delta\epsilon_{12} = 0.02\%$, all other $\Delta\epsilon_{ij}'s = 0$. The material model and initial conditions are the same as in the previous examples (assuming $\bar{c}_0 = 3$). The predicted shear bands are now oriented at 93° and 177° at a cumulative shear strain $\gamma_{12} = 0.76\%$, which is nearly twice the cumulative normal strain ϵ_{11} (in absolute value) required by the "in-axis" shearing simulation. For the band orientation of 93° the orientation of $\boldsymbol{m}$ is about 1°, while for the band orientation of 177° the orientation of $\boldsymbol{m}$ is 269°; in both cases, the angle between $\boldsymbol{n}$ and $\boldsymbol{m}$ is again 92°. Except for these new band orientations, the variations of the remaining parameters are the same as the "in-axis" shearing simulation.

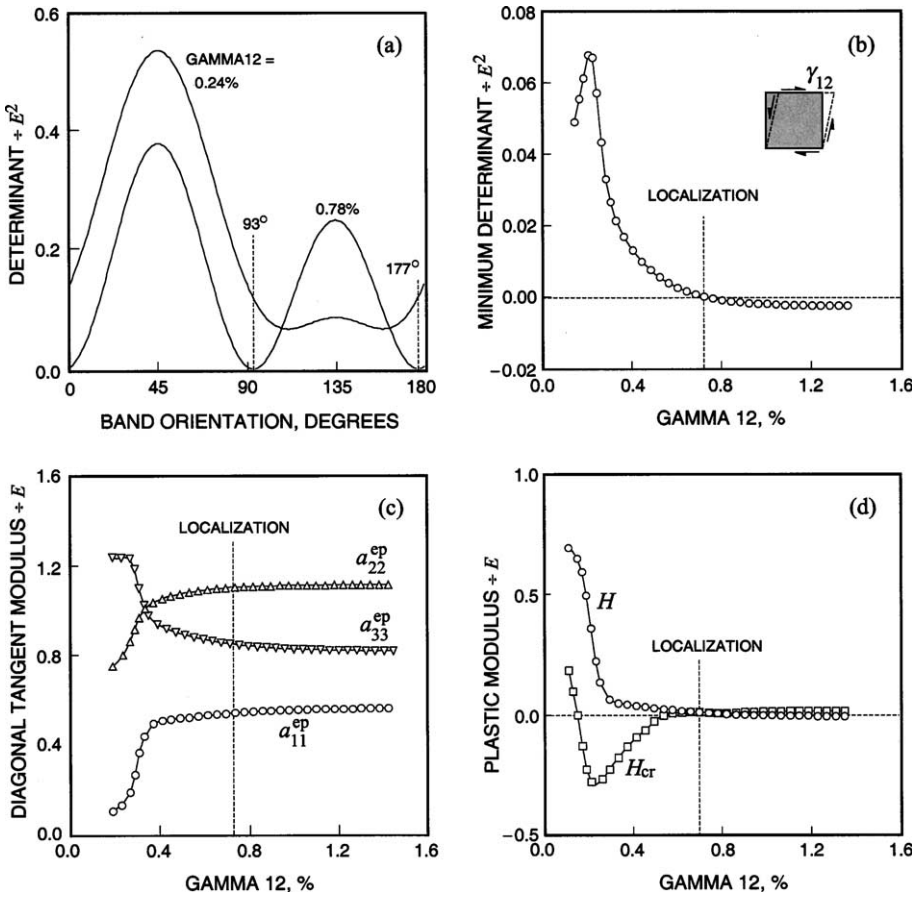

Fig. 12. Simple shear band, "out-of-axes" shear mode.

3.2. Dilatant shear band

We now bring the stress point to the dilatant side of the yield surface to investigate the onset of a dilatant shear band. Here we assume the initial stresses as $\sigma_{11} = \sigma_{22} = \sigma_{33} = -80$ kPa, less compressive than before, thus creating an initial condition in which the stress point lies well in the interior of the yield surface. We also lower the value of the exponent parameter μ slightly, from 0.5 to 0.45, for reason discussed later, but still take $\bar{c}_0 = 3.0$. Otherwise, all the remaining variables are the same as before.

Fig. 13 shows a dilatant shear band forming following the imposed local strain history $\Delta\epsilon_{11} = -0.010\%$, $\Delta\epsilon_{22} = 0.015\%$, all other $\Delta\epsilon_{ij}'s = 0$. In this case the element is stretched in the 2-direction faster than it is compressed in the 1-direction, and under a condition of plane strain this leads to an overall increase in volume. At a cumulative strain $\epsilon_{11} = -0.10\%$ the stress point comes in contact with the yield surface for the first time, and immediately the determinant of the localization function vanishes at band orientations of 67° and 113°, where the respective orientations of $\boldsymbol{m}$ are 118° and 62°. Thus, the angle between $\boldsymbol{m}$ and $\boldsymbol{n}$ is 51° so that $\boldsymbol{m} \cdot \boldsymbol{n} = 0.63$, affirming a dilatant shear band. Further plastic loading produces negative determinant values over some finite ranges of band orientations. Note that if $\mu = 0.5$ had been used, negative determinant values would have been obtained right at the onset of yielding.

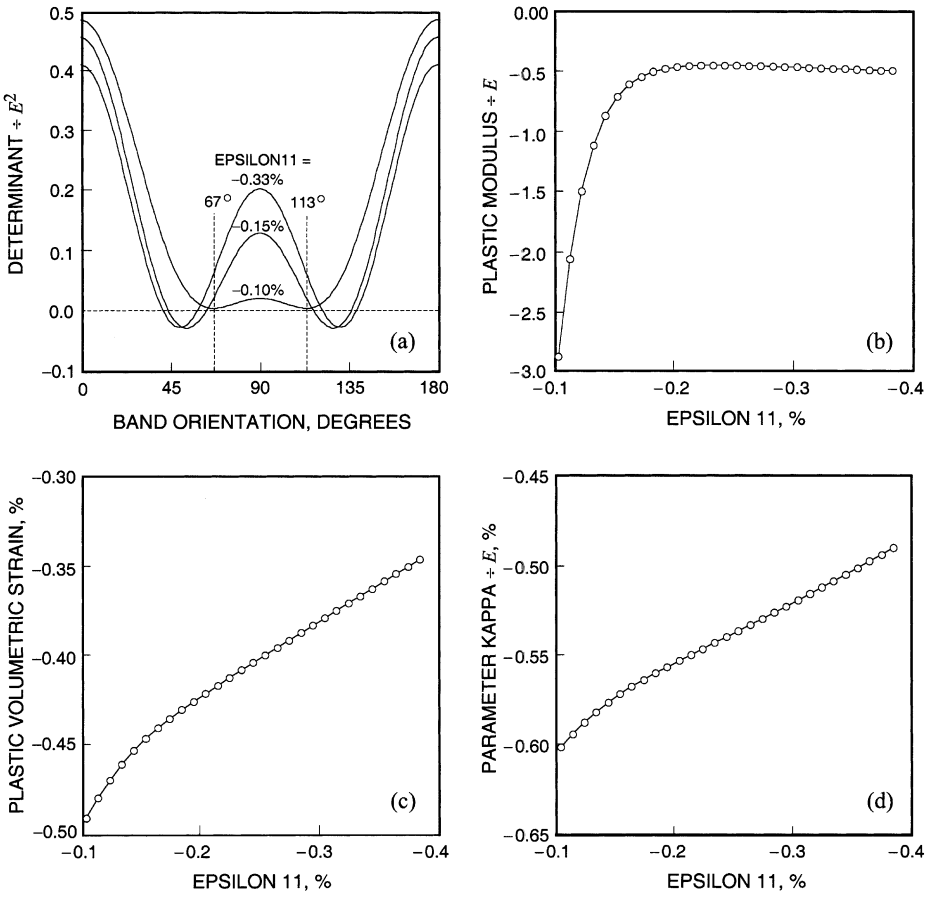

Fig. 13. Dilatant shear band.

As noted earlier the constitutive framework described above is very similar to the material model of [21] in which a conical failure surface was enhanced with a compression cap that expands with plastic compaction and shrinks with plastic dilation. In the model of [21] the failure surface was used as a yield surface that triggers the shrinking of the compression cap, a mechanism that is essentially replicated in Fig. 14. The present analysis illustrates the basic problem with this capped model formulation in that when yielding on the dilatant side the accompanying softening response associated with the shrinking of the cap could lead to an unstable material behavior. Figs. 13 and 14 show that on the dilatant side of the yield surface the plastic modulus is negative everywhere, thus enhancing bifurcation. The shrinking of the cap is precisely a feature that this model is designed to capture, yet it occurs in the regime of unstable behavior. Care must therefore be taken when interpreting the results of plastic yielding that occurs on the failure surface, see [25] for further examples.

3.3. Pure dilation band

For the plasticity model and material parameters considered we have been unable to reproduce a stress state that results in the formation of a pure dilation band. This does not imply that this failure mode is not possible—the shape of the yield and plastic potential surfaces obviously bears a strong influence on the

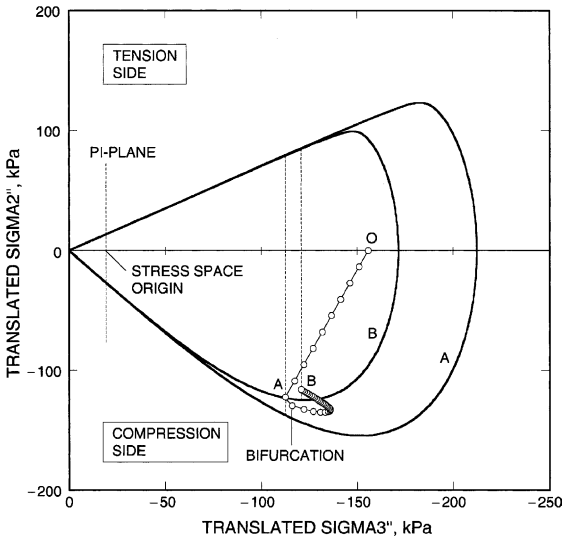

Fig. 14. Stress path for dilatant shear band simulation. Note: initial yield surface A shrinks to B as stress point moves from A to B; initial stress path OA is elastic, and actual contact points with the yield surface are away from the plane of the figure.

model predictions, and it is possible that the material parameters chosen inhibit the development of such a failure mode. To the best of our knowledge, no dilation band has been produced in laboratory sandstone samples (Aydin, personal communication).

4. Simulations with finite deformation

In this section we show that finite deformation effects can significantly influence the predicted bifurcation points. This effect has been previously demonstrated in [7] in the context of a boundary-value problem involving plane strain compression of dilatant frictional materials. In the present analysis we take a slightly different approach by assuming a given motion; we then compare the stages of motion at which the localization criterion is satisfied by the infinitesimal and finite deformation models. The motion considered is given by the mapping

$$x_1 = \Lambda_1 X_1, \qquad x_2 = \Lambda_2 X_2, \qquad x_3 = \Lambda_3 X_3, \tag{4.1}$$

where $\Lambda_1 = 1 - c(t)$, $\Lambda_2 = 1 + c(t)$, and $\Lambda_3 = 1$ are the principal stretches; $c(t) > 0$ is a scalar variable; and $\boldsymbol{X}$ and $\boldsymbol{x}$ are the position vectors in the undeformed and deformed configurations, respectively. The associated deformation gradient and left-Cauchy–Green deformation tensors are

$$\boldsymbol{F} = \begin{bmatrix} \Lambda_1 & 0 & 0 \\ 0 & \Lambda_2 & 0 \\ 0 & 0 & \Lambda_3 \end{bmatrix}, \qquad \boldsymbol{b} = \begin{bmatrix} \Lambda_1^2 & 0 & 0 \\ 0 & \Lambda_2^2 & 0 \\ 0 & 0 & \Lambda_3^2 \end{bmatrix}. \tag{4.2}$$

We view $c(t)$ as being applied in increments of Δc; the relative deformation gradient is then

$$\boldsymbol{f} = \frac{\partial \boldsymbol{x}_{n+1}}{\partial \boldsymbol{x}_n} = \begin{bmatrix} \lambda_1 & 0 & 0 \\ 0 & \lambda_2 & 0 \\ 0 & 0 & \lambda_3 \end{bmatrix}, \tag{4.3}$$

where $\lambda_1 = 1 - \Delta c/(1 + c(t_n))$, $\lambda_2 = 1 - \Delta c/(1 + c(t_n))$, and $\lambda_3 = 1$ are the principal stretches relative to the configuration at time t_n. In the linear (infinitesimal) theory the above motion defines a volume preserving "in-axis" plane strain simple shearing on the 12-plane. However, in the finite deformation theory the above motion is not volume preserving since $j = \det \boldsymbol{F} = \Lambda_1 \Lambda_2 \Lambda_3 \neq 1$.

We denote by $\boldsymbol{b}_n^{\mathrm{e}}$ the elastic left-Cauchy–Green deformation tensor at time t_n, with principal values equal to the squares of the elastic principal stretches $\Lambda_{i,n}^{\mathrm{e}}$, $i = 1, 2, 3$. By freezing the plastic flow we obtain the predictor value

$$\boldsymbol{b}_{n+1}^{\mathrm{e\,tr}} = \boldsymbol{f} \cdot \boldsymbol{b}_n^{\mathrm{e}} \cdot \boldsymbol{f}^{\mathrm{t}}. \tag{4.4}$$

In the absence of stress rotation this latter tensor has principal values equal to the squares of the trial elastic principal stretches

$$\Lambda_{i,n+1}^{\mathrm{e\,tr}} = \Lambda_{i,n}^{\mathrm{e}} \lambda_i, \quad i = 1, 2, 3. \tag{4.5}$$

Thus, the logarithmic strains are obtained as

$$\varepsilon_{i,n+1}^{\mathrm{e\,tr}} = \varepsilon_{i,n}^{\mathrm{e}} + \Delta\varepsilon_i, \quad i = 1, 2, 3, \tag{4.6}$$

where $\varepsilon_{i,n+1}^{\mathrm{e\,tr}} = \ln(\Lambda_{i,n+1}^{\mathrm{e\,tr}})$, $\varepsilon_{i,n}^{\mathrm{e}} = \ln(\Lambda_{i,n}^{\mathrm{e}})$, and $\Delta\varepsilon_i = \ln(\lambda_i)$. By using the logarithmic strains in principal axes we can then extend the return mapping algorithm of the infinitesimal theory to the regime of finite deformations. In the following we employ the return mapping algorithm of multiplicative plasticity theory [26] to integrate the stresses and hence identify the bifurcation points.

4.1. Simulation results

Assuming $E = 10$ MPa, a value 10 times smaller than that used for the sandstone examples to highlight the finite deformation effects, we compare in Figs. 15–17 the onset of a deformation band predicted by the infinitesimal and finite deformation models. At a value of $c(t) = 4.8\%$ the infinitesimal model shows localization occurring at band orientations of 42° and 138° (orientation of $\boldsymbol{n}$), where the corresponding orientations of $\boldsymbol{m}$ are 134° and 46°, respectively (Fig. 15a and b). In both cases the angle between $\boldsymbol{m}$ and $\boldsymbol{n}$ is 92°, and thus the two vectors are nearly perpendicular to each other. Note that the value of $c(t)$ for the infinitesimal model represents the normal compressive strain and the normal tensile strain in the 1- and 2-directions, respectively.

The finite deformation model predicts the onset of a deformation band at a value of $c(t) = 7\%$, much later than that predicted by the infinitesimal model (Fig. 15a and b). The band orientations are 40° and 140° (orientations of $\boldsymbol{n}$) reckoned with respect to the current configuration, where the corresponding orientations of $\boldsymbol{m}$ are 40° are 140°, respectively. In both cases, the angle between $\boldsymbol{m}$ and $\boldsymbol{n}$ is 96°, still nearly at right angle although slightly more on the compactive side. The compactive behavior noted is consistent with the fact that the Jacobian of the assumed motion is $j = 1 - (c(t))^2 < 1$, and so the imposed motion produces a volume decrease in the finite deformation formulation, thus enhancing the formation of a compactive shear band. Because of this volume decrease the finite deformation model predicts a larger compactive plastic volumetric strain, $\varepsilon_v^{\mathrm{p}} = \ln(\Lambda_1^{\mathrm{p}} \Lambda_2^{\mathrm{p}} \Lambda_3^{\mathrm{p}}) = \det \boldsymbol{F}^{\mathrm{p}}$, thus expanding the yield surface much further, whereas the infinitesimal model predicts steady-state values for the plastic volumetric strain and the parameter κ (Fig. 15c and d). The softening of the yield surface at higher levels of deformation noted in Fig. 15d is due to the reversal in the sign of the hardening law at a more advanced stage of loading, see (2.3).

Figs. 16 and 17 show the stress paths predicted by the two formulations on the σ_2'', σ_3''-meridian plane and the σ_1'', σ_2''-deviatoric plane, respectively. The figures clearly highlight the influence of the third stress invariant on the yield response of the material, with the stress paths on the deviatoric plane traversing yield surface cross-sections that vary in shape from nearly circular at lower deviatoric stresses to nearly

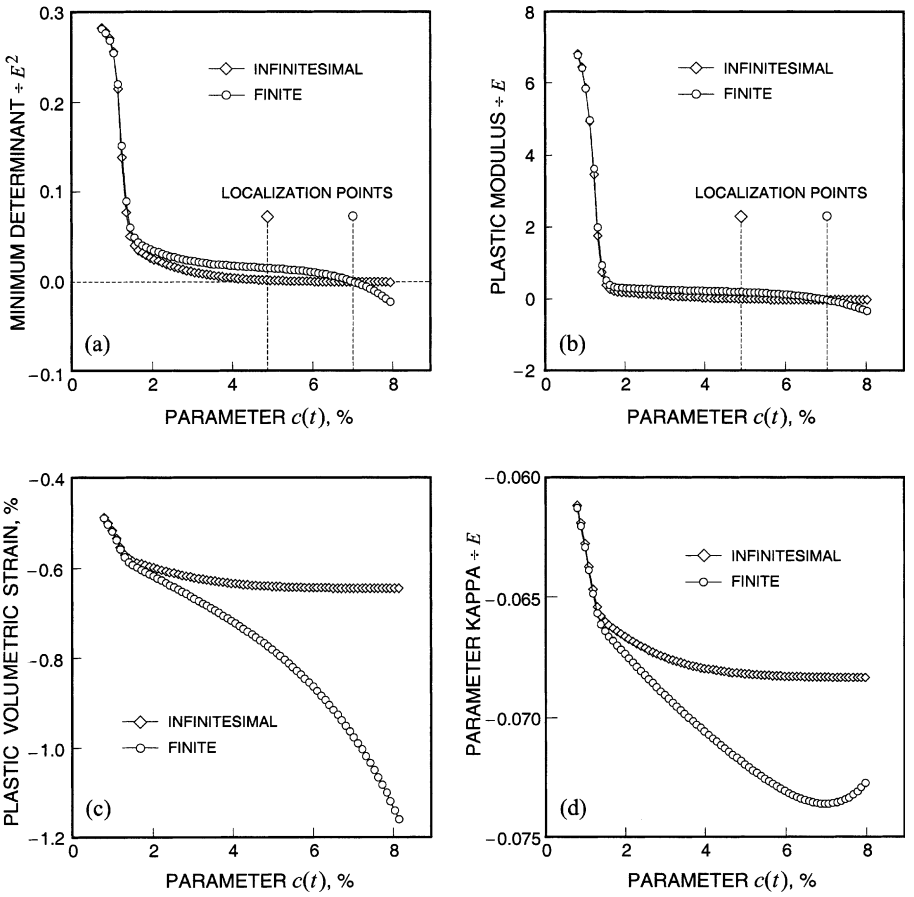

Fig. 15. Comparison of infinitesimal and finite deformation model predictions of "simple" shear band localized failure mode.

triangular at higher deviatoric stresses (Fig. 17). For the finite deformation plots the Kirchhoff stresses have been converted to Cauchy stresses by dividing the former by the Jacobian of the imposed motion so that the small and finite deformation stress paths can be superimposed on the same graph. Note that the final stress points for the two analyses (B and C for the small and finite deformation analyses) are nearly coincident yet the predicted bifurcation points are so far apart, suggesting a strong influence of the stress path on the localization points.

4.2. Constitutive and algorithmic tangent operators

Once again we compare the localization properties of the constitutive and algorithmic tangent operators relevant to the capture of the bifurcation points in the finite deformation regime. We recall the spectral representation of the constitutive tangent operator $\boldsymbol{\alpha}^{\mathrm{ep}}$ relating the Kirchhoff stress rate $\dot{\boldsymbol{\tau}}$ to the velocity gradient $\boldsymbol{l}$

$$\boldsymbol{\alpha}^{\mathrm{ep}} = \sum_{A=1}^{3}\sum_{B=1}^{3} a^{\mathrm{ep}}_{AB}\boldsymbol{m}^{(A)}\otimes\boldsymbol{m}^{(B)} + \frac{1}{2}\sum_{A=1}^{3}\sum_{B\neq A}\left(\frac{\tau_B-\tau_A}{b_B-b_A}\right)\left(b_B\boldsymbol{m}^{(AB)}\otimes\boldsymbol{m}^{(AB)} + b_A\boldsymbol{m}^{(AB)}\otimes\boldsymbol{m}^{(BA)}\right), \tag{4.7}$$

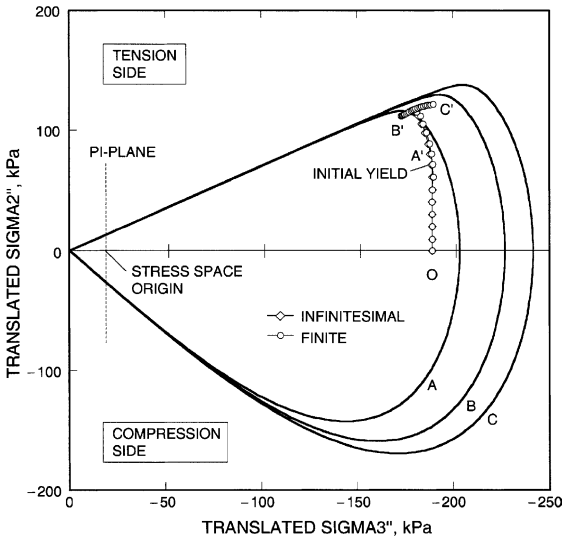

Fig. 16. Stress path for "simple" shear band simulation. Note: initial yield surface A expands to B in the infinitesimal formulation, and to C in the finite deformation formulation; initial stress path OA′ is elastic, and actual contact points A′, B′, C′ with the yield surface are away from the plane of the figure.

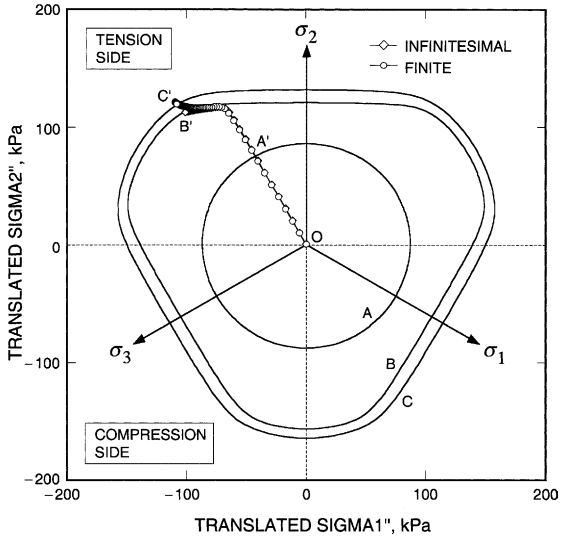

Fig. 17. Stress path for "simple" shear band simulation. Note: initial yield surface A expands to B in the infinitesimal formulation, and to C in the finite deformation formulation; initial stress path OA′ is elastic, and actual contact points with the yield surface are denoted as A′, B′ and C′.

where b_A is a principal value of the elastic left-Cauchy–Green deformation tensor $\boldsymbol{b}^e$. We also recall the spectral representation of the algorithmic tangent operator,

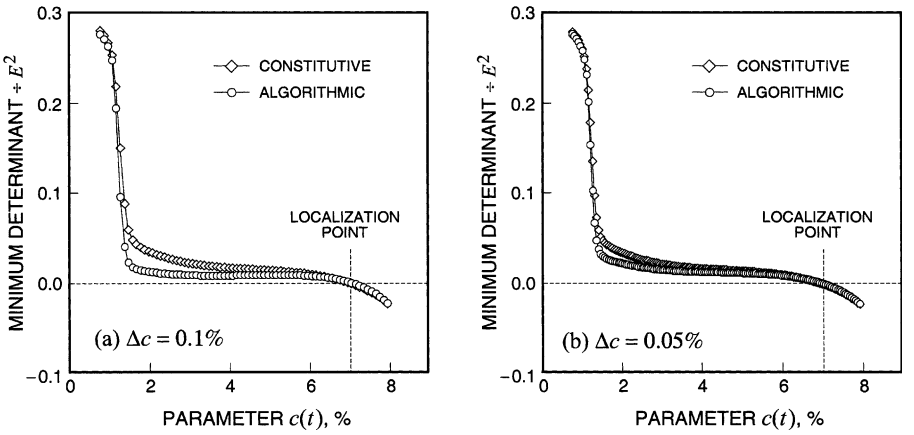

Fig. 18. Minimum determinants of constitutive and algorithmic Eulerian acoustic tensors.

$$\boldsymbol{\alpha} = \sum_{A=1}^{3}\sum_{B=1}^{3} a_{AB}\boldsymbol{m}^{(A)} \otimes \boldsymbol{m}^{(B)} + \frac{1}{2}\sum_{A=1}^{3}\sum_{B\neq A}\left(\frac{\tau_B - \tau_A}{\tilde{b}_B - \tilde{b}_A}\right)(\tilde{b}_B \boldsymbol{m}^{(AB)} \otimes \boldsymbol{m}^{(AB)} + \tilde{b}_A \boldsymbol{m}^{(AB)} \otimes \boldsymbol{m}^{(BA)}), \tag{4.8}$$

where $\tilde{b}_A$ is a principal value of the elastic left Cauchy–Green deformation predictor tensor $\boldsymbol{b}^{\mathrm{e\,tr}}$. The spectral directions are the same for both operators, and $\boldsymbol{\alpha}$ differs from $\boldsymbol{\alpha}^{\mathrm{ep}}$ only through the material tangent coefficient matrix $[a_{AB}]$ and the principal components of the tensors $\boldsymbol{b}^{\mathrm{e}}$ and $\boldsymbol{b}^{\mathrm{e\,tr}}$. Our goal now is to investigate how closely the two tangent operators predict the bifurcation points.

Fig. 18 plots the minimum determinants of the Eulerian acoustic tensor $\boldsymbol{a}$, with components

$$a_{ij} = n_k(\alpha_{ikjl} - \tau_{il}\delta_{jk})n_l, \tag{4.9}$$

using the constitutive and algorithmic tangent operators as given above. The search for the minimum value of the determinant was carried out numerically by sweeping all possible orientations of $\boldsymbol{n}$ in one-degree increments, and plotting the minimum as a function of the imposed deformation parameter $c(t)$. As expected, the two curves approach each other as Δc is applied in smaller increments. Worthy of note, however, is that the two tangent operators predict essentially the same localization points (zero determinant) even though the minima were significantly different early on during the loading history. For the case $\Delta c = 0.1\%$ the localization points predicted by the two tangent operators occurred during the same time step, while for the case $\Delta c = 0.05\%$ they occurred only one time step apart. We thus conclude that the algorithmic tangent operator is equally adequate for identifying the onset of localization in the finite deformation regime.

5. Closure

Throughout this paper we have constrained the parameters of the model in an effort to capture the localization properties of prototype geomaterials realistically. The constrained parameters included the elastic constants as well as those that influence the shape of the yield and plastic potential surfaces. The main free parameter of considerable interest is the plastic modulus H, along with its variation with the plastic strain. For rocks and other geomaterials the variation of the plastic modulus can significantly influence not only the emergence but also the nature of the deformation band. The measurement of the

plastic modulus in the laboratory must therefore be a prime object of any experimental program for validating the above localization model.

Acknowledgements

The assistance of graduate students Medji Sama and José Andrade, the input from Professor Atilla Aydin on the geological framework, and the constructive reviews of two anonymous reviewers are gratefully acknowledged. This work has been supported by National Science Foundation grant nos. CMS-97-00426 and CMS-03-24674, and US Department of Energy grant no. DE-FG02-03ER15454.

References

[1] R.I. Borja, A. Aydin, Computational modeling of deformation bands in granular media, I. Geological and mathematical framework, Comput. Methods Appl. Mech. Engrg., 2004, this issue.
[2] A. Aydin, R.I. Borja, P. Eichhubl, Geological and mathematical framework for failure modes in granular rock, in: G.D. Couples, H. Lewis, P. Meredith (Eds.), Relationships Between Fracture Damage and Localisation, Geological Society of London Special Publications, accepted.
[3] G. Mavko, T. Mukerji, J. Dvorkin, The Rock Physics Handbook. Tools for Seismic Analysis of Porous Media, Cambridge University Press, Cambridge, 1997.
[4] A.S. Vesic, G.W. Clough, Behavior of granular materials under high stresses, J. Soil Mech. Found. Div., ASCE 94 (1968) 661–668.
[5] D.M. Wood, Soil Behaviour and Critical State Soil Mechanics, Cambridge University Press, Cambridge, 1990.
[6] J.W. Rudnicki, J.R. Rice, Conditions for the localization of deformation in pressure-sensitive dilatant materials, J. Mech. Phys. Solids 23 (1975) 371–394.
[7] R.I. Borja, Bifurcation of elastoplastic solids to shear band mode at finite strain, Comput. Methods Appl. Mech. Engrg. 191 (2002) 5287–5314.
[8] R.I. Borja, K.M. Sama, P.F. Sanz, On the numerical integration of three-invariant elastoplastic constitutive models, Comput. Methods Appl. Mech. Engrg. 192 (2003) 1227–1258.
[9] R.I. Borja, Algorithm for a class of three-invariant elastoplastic constitutive models suitable for the analysis of deformation bands in geomaterials, in: E. Oñate, D.R.J. Owen (Eds.), Proceedings of the VII International Conference on Computational Plasticity (COMPLAS 2003), CIMNE, Barcelona (in CD Rom).
[10] W.A. Olsson, Theoretical and experimental investigation of compaction bands in porous rock, J. Geophys. Res. 104 (1999) 7219–7228.
[11] K.A. Issen, J.W. Rudnicki, Conditions for compaction bands in porous rock, J. Geophys. Res. 105 (2000) 21529–21536.
[12] X. Du Bernard, P. Eichhubl, A. Aydin, Dilation bands: a new form of localized failure in granular media, Geophys. Res. Lett. 29 (4) (2002) 2176, doi:10.1029/2002GL015966.
[13] M.K. Kim, P.V. Lade, Single hardening constitutive model for frictional materials I. Plastic potential function, Comput. Geotech. 5 (1988) 307–324.
[14] P.V. Lade, M.K. Kim, Single hardening constitutive model for frictional materials II. Yield criterion and plastic work contours, Comput. Geotech. 6 (1988) 13–29.
[15] P.V. Lade, M.K. Kim, Single hardening constitutive model for frictional materials III. Comparisons with experimental data, Comput. Geotech. 6 (1988) 31–47.
[16] G. Perrin, J.B. Leblond, Rudnicki and Rice's analysis of strain localization revisited, J. Appl. Mech. 60 (1993) 842–846.
[17] G. Schickert, H. Winkler, Results of tests concerning strength and strain of concrete subjected to multiaxial compressive stresses, Deutscher Ausschus fur Stahlbeton 277, 1977, Berlin.
[18] H. Kupfer, H.K. Hilsdorf, H. Rusch, Behavior of concrete under biaxial stresses, J. Am. Concr. Inst. 66 (1969) 656–666.
[19] M.E. Tasuji, F.O. Slate, A.H. Nilson, Stress–strain and fracture of concrete in biaxial loading, J. Am. Concr. Inst. 75 (1978) 306–312.
[20] H. Aschl, D. Linse, S. Stoeckl, Strength and stress strain behavior of concrete under multiaxial compression and tension, in: Proceedings of the 2nd International Conference Mechanical Behavior of Materials, Boston, MA, 1976, pp. 102–117.
[21] F.L. DiMaggio, I.S. Sandler, Material model for granular soils, J. Engrg. Mech. Div., ASCE 97 (1971) 935–950.
[22] J. Maso, J. Lerau, Mechanical behavior of Darney sandstone in biaxial compression, Int. J. Rock Mech. Min. Sci. Geomech. Abstr. 17 (1980) 109–115.

[23] J.C. Simo, R.L. Taylor, Consistent tangent operators for rate-independent elastoplasticity, Comput. Methods Appl. Mech. Engrg. 48 (1985) 101–118.
[24] J. Desrues, R. Chambon, Shear band analysis and shear moduli calibration, Int. J. Solids Struct. 39 (2002) 3757–3776.
[25] T.Y. Lai, R.I. Borja, B.G. Duvernay, R.L. Meehan, Capturing strain localization behind a geosynthetic-reinforced soil wall, Int. J. Numer. Anal. Methods Geomech. 27 (2003) 425–451.
[26] J.C. Simo, Algorithms for static and dynamic multiplicative plasticity that preserve the classical return mapping schemes of the infinitesimal theory, Comput. Methods Appl. Mech. Engrg. 99 (1992) 61–112.